Visible light-driven photocatalytically active g-C$_3$N$_4$ material for enhanced generation of H$_2$O$_2$

Zedong Zhu[a], Honghui Pan[a], Muthu Murugananthan[b], Jianyu Gong[a], Yanrong Zhang[a],*

[a] Environmental Science Research Institute, Huazhong University of Science and Technology, Wuhan 430074, PR China
[b] Department of Chemistry, PSG College of Technology, Peelamedu, Coimbatore 641004, India
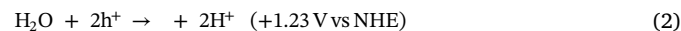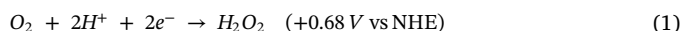
ARTICLE INFO

ABSTRACT

Reduced g-C$_3$N$_4$ material was prepared by a thermal treatment of g-C$_3$N$_4$ in presence of NaBH$_4$ under N$_2$ atmosphere. The prepared catalyst material was characterized by using elemental analyzer, FTIR and XPS and the analysis showed that the reduction treatment created nitrogen vacancies followed by a formation of functional group C≡N owing to a break-up reaction in the pyridine nitride of a s-triazine-C$_3$N$_4$. The findings of UV–vis DRS and DFT calculation revealed that the formed functional group C≡N results in a narrowed energy band gap owing to positive shift in the conduction band as well as valence band. The downshift observed in the valence band level made the catalyst material with a feature of visible light-driven water oxidation capacity, that was confirmed by the electron and hole sacrifice and ·OH trapping-EPR techniques. The intermediate energy level within the band gap of g-C$_3$N$_4$ originated from the vacancies caused an extended absorption, especially to the visible region. The analysis of PL emission spectrum confirmed that the reduction treatment could facilitate the spatial separation of photo-excited electron and hole, and enhance the charge transfer as well. RDE studies showed that the selective production of H$_2$O$_2$ by two-electron reduction of O$_2$ was a predominant reaction step using the reduced g-C$_3$N$_4$. The reduced g-C$_3$N$_4$ prepared at 370 °C exhibited an efficient visible light driven catalytic performance on H$_2$O$_2$ production (170 μmol/L h^{-1}) from pure H$_2$O and O$_2$ at ambient atmosphere in the absence of organic electron donors. The solar-to-H$_2$O$_2$ chemical conversion efficiency and apparent quantum yield approached to ∼0.26%, ∼4.3%, respectively. In addition, the experimental results obtained on recycling of the prepared g-C$_3$N$_4$ evidenced the photocatalytic stability of the material.

1. Introduction

H$_2$O$_2$, known as an effective redox reagent, is widely used for many applications, such as water purification, antibacterial, bleaching, cleaning agents, organic compound synthesis and fuel cells [1]. The photocatalytic approach for production of H$_2$O$_2$ is superior to other existing techniques such as anthraquinone method [2], which are not green due to high energy consumption. Also, a direct synthesis route from H$_{2(g)}$ and O$_{2(g)}$ using noble metals and their alloy catalysts involves risk and it is dangerous at times, due to explosive nature of the gases containing H$_2$/O$_2$ mixture.

In the earlier attempts, widely made on inorganic-based semiconductor photocatalysts such as TiO$_2$ system, H$_2$O$_2$ is generally produced via O$_2$ reduction step on conduction band from O$_2$-saturated water under UV light irradiation. The photo-generated electron (e$^-$) promotes two-electron reduction of O$_2$ and generates H$_2$O$_2$ (Eq. 1), whereas the photo-excited hole oxidizes the water or deliberately accommodated the electron and proton donor such as alcohol (Eqs. 2 and

3). However, the efficiency for H$_2$O$_2$ production is very poor as the TiO$_2$ shows less selectivity on H$_2$O$_2$ generation and also, the generated H$_2$O$_2$ gets decomposed by the irradiated UV light (λ < 400 nm) [3] during the photocatalytic reaction process.

$$O_2 + 2H^+ + 2e^- \rightarrow H_2O_2 \quad (+0.68\,V \text{ vs NHE}) \tag{1}$$

$$H_2O + 2h^+ \rightarrow \quad + 2H^+ \quad (+1.23\,V \text{ vs NHE}) \tag{2}$$

$$R\text{-}CH_2OH + 2h^+ \rightarrow R\text{-}CHO + 2H^+ \quad (+0.22\,V \text{ vs NHE}) \tag{3}$$

Graphitic Carbon Nitride (g-C$_3$N$_4$) is a metal-free polymeric photocatalyst, fabricated from tri-s-triazine units linked by planar amino groups (Fig. S1) [4]. Due to its visible-light driven photocatalytic nature and robust characteristic behaviours [5], the g-C$_3$N$_4$ based semiconductor has drawn increasing attention as a promising alternative for H$_2$ production [3,6], CO$_2$ reduction [7,8] and pollutants degradation [9,10], and especially for H$_2$O$_2$ production [4,11,12] in recent years. The selectivity in photocatalytic method towards H$_2$O$_2$ generation is probably due to the formation of 1,4-endoperoxide species on the g-

---

C_3N_4 surface, which actually gets transformed as H_2O_2 molecule [2,5,13]. However, the performance of pristine g-C_3N_4 in water media was reported to be poor, as a result of fast intrinsic recombination of the photoexcited carriers caused by the π-π conjugated electronic system of g-C_3N_4 framework [14]. Also, the low valence band (VB) energy level, that lies approximately at $+1.4\,V$ (vs NHE, pH = 7), is perhaps an insufficient potential to meet the water oxidation (ca.0.8 V, pH = 7) [2,15,16]. Incorporating electron-deficient or π-conjugated monomer into the lattice network of g-C_3N_4 [13,14,17–20], which simultaneously pulls down both the conduction band (CB) and VB position, and inhibits the recombination of photoexcited electron and hole pairs, promotes its photocatalytic activity for H_2O_2 generation from pure water and O_2 gas.

A self-modification approach of creating homogeneous nitrogen or carbon vacancies is an alternative strategy to achieve a desired band structure of g-C_3N_4 having enhanced photocatalytic activity [12,19,21–23]. On the other hand, developing defects in the lattice structure significantly improves the photocatalytic activity of material [4]. The g-C_3N_4 is a typical n-type material since it contains many electron donor ($-NH/NH_2$) groups in the lattice structure. The implantation of a strong electron acceptor functional group, such as C≡N could separate the photogenerated electron and hole pairs [22] and in turn reduce the energy band gap along with a positive shift in the CB and VB positions, thereby enhance the photocatalytic activity of the material.

In this work, the reduction of g-C_3N_4 in the presence of $NaBH_4$ was carried out by a thermal treatment to form C≡N functional groups. An oligomer g-C_3N_4 prepared at a temperature of $450\,°C$ was used as a precursor to undergo a self-modification study as the VB energy level is very close to that of water oxidation [2,3,13,15].

2. Experimental

2.1. Preparation of reduced g-C_3N_4

The pristine g-C_3N_4 was prepared by thermal polymerization of melamine at a desired temperature ranging in between 425 and $550\,°C$ for 4 h with a ramping rate of $5\,°C/min$ in an ambient atmosphere. Thereupon, it was washed with hot deionized water $(80\,°C)$ to remove melamine and dried in vacuum. The g-C_3N_4-x represents pristine g-C_3N_4 prepared at the respective heating temperature of x.

The reduced catalyst was prepared by using the g-C_3N_4-450 as a precursor. It was thoroughly blended with $NaBH_4$ (weight ratio 1:5) in a mortar, and then thermally treated at various desired temperatures (from 300 to $400\,°C$) in N_2 atmosphere for 30 min. After a natural cooling in open atmosphere, the product was rinsed thrice with hot deionized water $(80\,°C)$. R_x-CN represents the reduced g-C_3N_4-450 at the respective reduction temperature referred by x.

2.2. Characterization

The morphology study was performed with a field emission scanning electron microscope (FE-SEM; NANOSEM 450, FEI) operating at an accelerating voltage of 30 kV. The phase and crystal structure of the obtained samples were examined by X-ray diffraction technique (XRD; Rigaku Ultima IV, Rigaku) equipped with Cu $K\alpha$ radiation (40 kV, $\lambda = 1.5406\,Å$). The absorbance of the samples was recorded on a UV–vis diffuse reflectance spectrometry (UV–vis DRS, UV-2600, Shimadzu, Japan) at room temperature. The photoluminescence spectra (PL) were measured with a fluorescence spectrophotometer (Jasco FP-6500, Japan). The C/N atomic ratio of pristine and reduced g-C_3N_4-450 was determined using a Vario Microcube Elemental analyzer. Fourier Transform Infrared (FTIR) spectra were recorded using a VERTEX 70 spectrometer. The analyte samples were mixed with KBr and pressed to form pellets for the detection (1 mg sample, 200 mg KBr, hand press at 10 MPa). The surface chemical analysis was carried out by X-ray photoelectron spectroscopy (XPS; AXIS-ULTRA DLD-600W, Kratos). The

XPS elemental analysis was corrected based on the C 1s peak at 284.6 eV.

2.3. Studies on photocatalytic activity

The H_2O_2 production experiments were carried out by an addition of 0.1 g photocatalyst in 100 mL deionized water. After stirring in dark for 2 h, the suspension was exposed to light irradiation with a 300 W Xenon lamp (PLS-SXE 300, Perfect light, China) under a constant stirring. A cut-off filter was employed to achieve visible-light $(\lambda > 420\,nm)$ irradiation. During the irradiation, about 5 mL of suspensions was sampled and filtered in every 30 min duration, to remove the suspended photocatalytic materials. The amount of H_2O_2 generated was determined by performing a redox titration against $KMnO_4$ reagent solution [13].

2.4. Detection of ·OH

The detection of ·OH experiment was carried out as follows. Initially, 0.1 g photocatalyst was suspended in an aqueous solution of 2 mM benzoic acid [24], and the suspension was stirred in dark for 2 h followed by light irradiation under a constant stirring. At a reaction interval of 2 h, the solution was subjected to a detection of the p-hydroxybenzoic acid by using high performance liquid chromatography (HPLC; LC-15C, Shimadzu, Japan) equipment with an UV detector and a reverse phase SinoChrom ODS-BP-8 column (150 × 4.6 mm).

The ·OH was further examined by an electron paramagnetic resonance (EPR; EMXnano, Bruker) technique employing 5,5-dimethylpyridine N-oxide (DMPO) as a spin-trapping agent. A 0.02 g of catalyst was added to a container having 20 mL of 0.16 M DMPO solution prepared using deionized water. The container was kept under visible light irradiation for 5 min, then the filtrate solution was subjected to the test at room temperature.

2.5. Calculation methodology

The calculations in the present study are in the density functional theory (DFT) level within the Gaussian 09 program, using the density functional B3LYP. Geometries were optimized using the 6-31G (d, p) basis sets. A two dimensional (2D) melem unit ($H_6C_6N_{10}$) was used to represent the incomplete polycondensation of g-C_3N_4-450, and a simple melem-CN ($H_{14}C_{14}N_{22}$) mode was used to clarify the impact of C≡N functional groups on the electronic structure of g-C_3N_4-450.

2.6. Electrochemical measurements

Rotating disk electrode (RDE) studies were conducted using an electrochemical workstation (CHI760, Instruments) coupled with a rotating disk electrode system (Pine Research Instrumentation, USA). The three-electrode cell system was consisting of a reversible hydrogen electrode (RHE) and a Pt wire electrode as the reference and counter electrode, respectively. The working electrode was prepared as follows: ultrasonication of 5 mg of the as-prepared sample with 1 mL 0.1% Nafion solution (diluted with isopropyl alcohol). 7.8 μL of homogeneous ink was dropped uniformly on to a glassy carbon electrode (diameter of 5 mm) and the electrode was dried at room temperature. The linear polarization curves were obtained in an O_2-saturated 0.1 M K_2SO_4 solution with a scan rate $10\,mV\,s^{-1}$ after O_2 bubbling for 5 min period.

Electrochemical impedance spectroscopy (EIS) and Mott-Schottky plots were done with an electrochemical workstation (CS310, CoorrTest, China), and the detailed procedures were described in our previous publication [25]. The measurements were carried out in a conventional three-electrode cell using the catalyst, SCE and Pt mesh as working, reference, and counter electrodes, respectively. The electrolyte used was 0.5 M Na_2SO_4 aqueous solution. The substrate used for

working electrode was FTO glass material [13]. Catalyst (50 mg) was mixed with acetone (2 mL), and ultrasonicated for 30 min. The mixture was put onto the FTO and annealed at 350 °C for 30 min in atmospheric air for strong adhesion. EIS measurements were performed between 0.1 MHz and 0.01 Hz with 10 mV AC amplitude at −0.05 V DC potential on each sample with a geometrical area of 2 cm². The perturbation signal for Mott-Schottky measurements was performed at a frequency of 1000 Hz.

2.7. Determination of solar-to-H_2O_2 chemical conversion (SCC) efficiency and apparent quantum yield (AQY)

The efficiency of SCC was measured using a borosilicate glass bottle which contains pure water sample (100 mL) with a dosage of the catalysts 400 mg under 1 atm pressure of O_2, and the other experimental conditions were similar to the one mentioned in the Section 2.3. The average intensity of irradiation was determined by using a spectro-radiometer (PL-MW2000, China). The SCC efficiency was calculated by the equation described below [18].

SCC Efficiency

$$= \frac{[\Delta G \text{ for } H_2 \ O_2 \text{ generation } (J \ mol^{-1})][H_2 \ O_2 \text{ formed (mol)}]}{[\text{total input energy } (w)][\text{reaction time } (s)]}$$

The AQY was measured under similar conditions of the SCC apart from the irradiation parameters i.e. the intensity and the wavelength regions. The irradiation of 420 nm was lasted for 60 min duration. The AQY was calculated using the following equation [21].

$$AQY = \frac{[N(H_2O_2) \times 2]}{[N(photos)]} \times 100\%$$

3. Results and discussion

3.1. Structure and morphology

The XRD patterns as shown in Figs. 1 and S2 confirmed the formation of g-C_3N_4, and the peaks of 2θ angle located at 13.2° and 27.3° can be ascribed to the repeat structure of in-plane and the interlayer stacking of stratified structure [26,27]. The impact of reduction treatment at a fixed temperature viz. 300, 350, 370 and 400 °C on the basic 2D conjugated structure of graphitic carbon nitride was minimum as shown in Fig. 1. In addition, with an increase of operating temperature, the impure peaks at 6°, 31° and the multiple peaks at around 27° gradually disappeared for both the pristine and the reduced photocatalysts. It could be ascribed to the structural change of melem during the process of reduction treatment [28,29]. The melem should be ring-opened [22] rather than re-polymerized, as the change started at
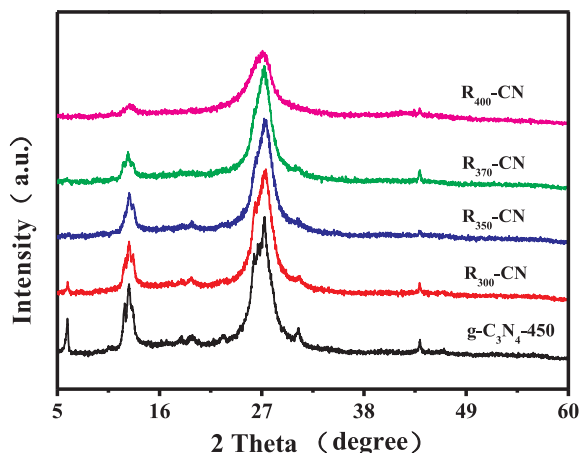

Fig. 1. XRD patterns of pristine g-C_3N_4-450 and R_x-CN (x = 300, 350, 370 and 400).
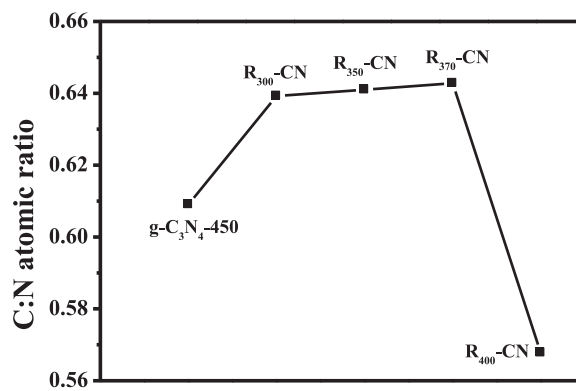

Fig. 2. Elemental analysis of pristine g-C_3N_4-450 and R_x-CN (x = 300, 350, 370 and 400).

370 °C, while the possibility for re-polymerization could not take place until an operating temperatures higher than 389 °C [3,28]. On the other hand, the particulate morphology and size of the pristine g-C_3N_4-450 and the R_{370}-CN were almost identical as depicted in Fig. S3.

3.2. Investigation on defects of the reduced catalyst

As shown in elemental analysis (Fig. 2), a prominent difference in the C/N atomic ratio between the reduced catalyst and the pristine g-C_3N_4-450, and the two different trends of operating temperature against above and below of 370 °C were observed. The ratio for $R_{300-370}$-CN was ~0.642, higher than that (0.607) of its pristine precursor. There was a mild hike in the C/N atomic ratio value as the reduction process temperature went up and however, the value went down as ~0.566 for 400 °C, which was even lower than that of the pristine g-C_3N_4-450 precursor. The difference in the C/N atomic ratio observed for the reduced catalysts prepared at various conditions showed the development of defect in the g-C_3N_4-450 upon a thermal treatment in the presence of NaBH₄. Furthermore, as the report suggested, the preferential loss of N and C atoms occurred at operating temperatures between 300–370 °C [22], and a higher operating temperature 400 °C, respectively. The defects developed in the reduced g-C_3N_4-450 could be due to the interaction of the pristine g-C_3N_4-450 with active hydrogen during the reduction process. It has been experimentally confirmed that H_2 and active hydrogen could reduce lattice N in g-C_3N_4 into NH₃ and consequently lead to the defects formation [22,23]. Considering the behavior of endothermic reaction, the N lattices except the nitride (N3) located in the center (Fig. 3) were expected to get reduced to NH₃ by the active hydrogen. The reduction reactions taken place at tertiary nitride (N1) would create nitride vacancies, while at pyridine nitride (N2) would cleave the s-triazine heterocycles in g-C_3N_4-450 yielding C≡N group, both of which, emerged as main defects upon the reduction treatment. The former reaction would cause an increase in C/N atomic ratio, whereas the latter a decrease in C/N atomic ratio due to the loss of C/N atoms ratio of 2:3, which was greater than that of the pristine g-C_3N_4-450 (~3:5).

The formation of C≡N functional group upon the reduction treatment of g-C_3N_4-450 was further examined by FTIR spectra analysis. As shown in Fig. 4, the three typical characteristic peaks located at 3000–3500, 1000–1700 and 810 cm⁻¹, could be ascribed to the vibration of N−H bonds, aromatic C−N heterocycles and s-triazine subunits [22,30], respectively. However, upon the reduction treatment, a new vibration band at 2180 cm⁻¹, belonging to C≡N triple bonds [31], appeared in the spectra and the peak intensity gradually increased with the operating temperature increasing from 300 to 400 °C. The formation of C≡N groups meant the opening of the s-triazine subunits in g-C_3N_4-450 (Fig. 3) [22], which was in well agreement with the decrease in the intensity of its characteristic peak at 810 cm⁻¹. Particularly, the intensity of this peak drastically decreased at a temperature of 400 °C,
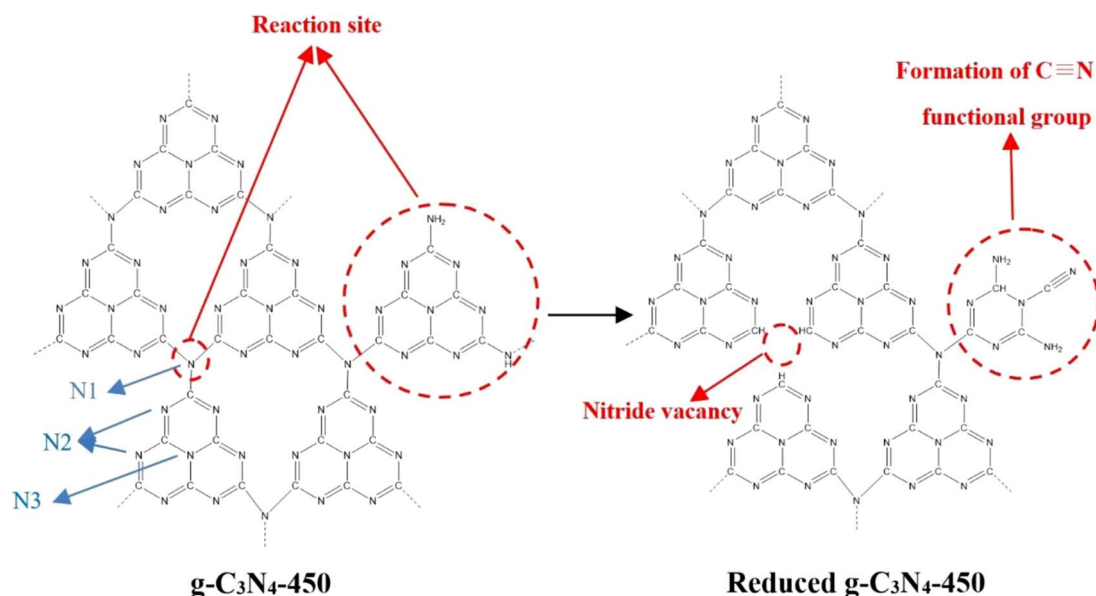
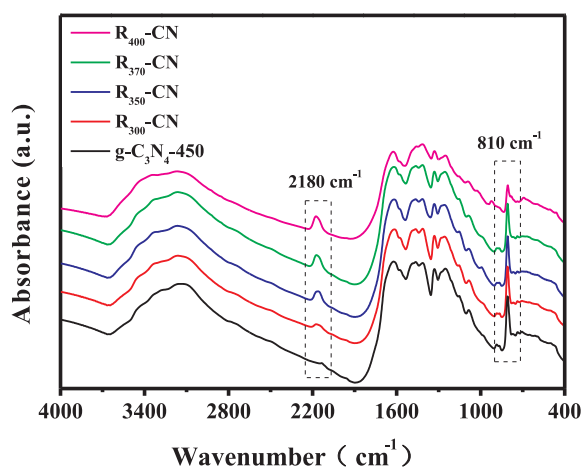**Fig. 3.** The probable reaction of g-C₃N₄-450 treated with NaBH₄.

Fig. 4. FTIR spectra of pristine g-C₃N₄-450 and R$_x$-CN (x = 300, 350, 370 and 400).

showing that the opening of s-triazine heterocycles in g-C₃N₄-450 was a dominant reaction at this temperature.

XPS is a quantitative spectroscopic technique with high sensitivity that measures the chemical state of the elements existing within the material and was used to clarify the information with respect to the defects. According to the XPS results shown in Fig. S4, Table S1 and Table S2, both pristine and reduced g-C₃N₄-450 consisted of three common nitrogen species with N 1s peaks of 401.0, 399.6 and 398.0 eV, against C–NH$_x$ and C≡N, N-(C)₃ and C–N=C bonding structures, respectively [12,31–33]. The peak area at 401.0 eV increased (Table S1) with the increase in the treatment temperature, which was solely originated from the C≡N but not C–NH$_x$ bonding structures, based on the FTIR results from Fig. 4. On the other hand, the N-(C)₃ ratio that decreased from 47.5% to 30.9% as shown in Table S1, could theoretically be ascribed to the removal of both N1 and N3 in g-C₃N₄-450. However, the larger endothermic energy reacted with H₂ excluded the removal of N3 [23], confirmed the N1 as reduction site to form the nitrogen vacancies (Fig. 3).

Three common C 1s peaks belonging to C–O (289.5 eV), N–C=N (287.5 eV) and C=C (284.6 eV) were observed for both pristine and reduced samples. Usually, the presence of functional groups such as C–O etc. in pristine g-C₃N₄ network is inevitable. However, the intensity of C–O peak that got lowered with the catalyst subjected to

NaBH₄ treatment (Table S2), unlike the intensity of C=C peak, indicated the breaking of few C–N bonds [34]. Beyond that, an additional C 1s peak at 286.5 eV assigned to N=CH–N bonding structure [12,13], was observed for the reduced samples. The intensity of this peak increased from 13.6% to 19.8% with the reduction temperature from 300 to 400 °C, accompanying a decrease of N–C=N coordination from 54.1% to 39.4% (Table S2). The breaking of N-(C)₃ would lead to the formation of N=CH-N that consequently lower the N–C=N, thus the reduction reaction occurred at the N1 site was further confirmed. Moreover, the increase of C≡N group from 14.2% up to 22.7% (Table S1) could be attributed to the cleavage of the s-triazine heterocycles (Fig. 3) in the g-C₃N₄-450. The interpretations made by XPS were in good agreement with those from the elemental analysis mentioned above.

3.3. Activity of the reduced g-C₃N₄-450 on photocatalytic generation of H₂O₂

As shown in Fig. 5, the pristine g-C₃N₄-450 could hardly generate H₂O₂ at ambient atmosphere under visible light irradiation, whereas a great enhancement was achieved upon the development of defects. The efficiency of photogeneration of H₂O₂ got increased with the reduction temperature starting from 300 to 370 °C, followed by a fall with a
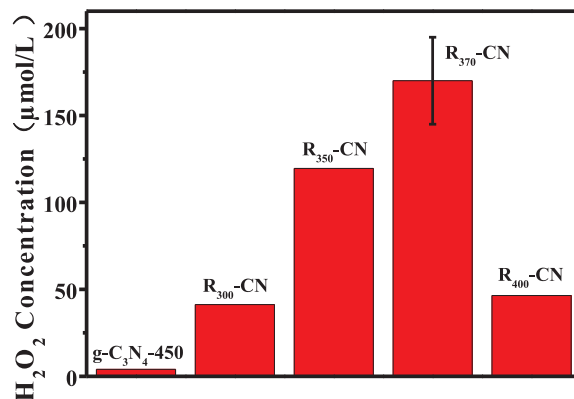

Fig. 5. Photocatalytic generation of H₂O₂ by the respective photocatalyst of g-C₃N₄-450 and R$_x$-CN (x = 300, 350, 370 and 400) from pure water and ambient atmosphere under visible light irradiation for 1 h.

further increase of temperature to 400 °C. The control experiments carried out in the presence of N_2 and O_2 gas aeration into reaction media confirmed that the generation of H_2O_2 molecule was originated from the reduction of O_2 (Fig. S5). The enhanced generation of H_2O_2 only to an extent of ~ 34% with O_2 gas aeration was mainly because of oxidation of H_2O molecule at VB during the photocatalytic reaction and this was an rate determining step, which limited further enhancement in the generation of H_2O_2, irrespective of the concentration of O_2. In addition, the minimum quantity of H_2O_2 generated with N_2 aeration might be from reduction of the residual quantity of O_2 in the working solution. The maximum yield of H_2O_2 was observed to be 170 µmol/ L h^{-1} against the R_{370}-CN from pure H_2O and O_2 at ambient atmosphere. The calculated efficiencies of SCC and AQY towards the photogeneration of H_2O_2 at the catalyst were ~ 0.26% and ~ 4.3%, respectively. The AQY was comparable with other catalysts reported such as La/Cr co-doped CaTiO$_3$ hollow cubes showing 2.41% [35], and (C$_{ring}$)-C$_3$N$_4$ showing 5% [17]; Also, the performance of SCC efficiency was fair and comparable with other catalysts, such as g-C$_3$N$_4$/PDI/rGO showing 0.2% [18], g-C$_3$N$_4$/BDI showing 0.13% [13], and g-C$_3$N$_4$/MTI showing 0.18% [36].

It is important to note that under similar reaction conditions, the rate of H_2O_2 generation over the R_{370}-CN was (17 µmol h^{-1}) more than that over other g-C$_3$N$_4$-based catalysts such as Cv-g-C$_3$N$_4$ (9.2 µmol h^{-1}), g-C$_3$N$_4$-PDI$_{51}$-rGOs (1.2 µmol h^{-1}), g-C$_3$N$_4$-NiFeO (1.8 µmol h^{-1}), and 3DOM g-C$_3$N$_4$-PW$_{11}$ (2.4 µmol h^{-1}) [37]. The better generation of H_2O_2 observed in the case of R_{370}-CN made it a promising candidate for visible light-driven photocatalytic generation of H_2O_2 without organic electron donors.

3.4. Confirmation of the selective two-electron reduction of O_2 by the reduced g-C$_3$N$_4$-450

RDE studies were performed to investigate the reaction pathway of O_2 reduction. The RDE curves obtained against the R_{370}-CN at various rpm speed viz. 400, 600, 900, 1200, 1600, and 2000 are shown in Fig. 6. The number of electrons involved in the process of O_2 reduction was calculated by Koutecky-Levich (K-L) equation as described below.

$$1/j_{lim} = 1/j_{lev} + 1/j_k$$

where, J_{lim}, J_{lev} and J_k are the limiting current, Levich current and kinetic current, respectively [38].

From the K-L plots of the experimental results, the electron transfer number n for the O_2 reduction was 2.42 for R_{370}-CN (Fig. S6), which was closer to the theoretically calculated value 2. It suggested that the selective photogeneration of H_2O_2 was the predominant reaction.

To elucidate the mechanism of the enhanced photocatalytic activity achieved upon the reduction treatment, the characterization of both the
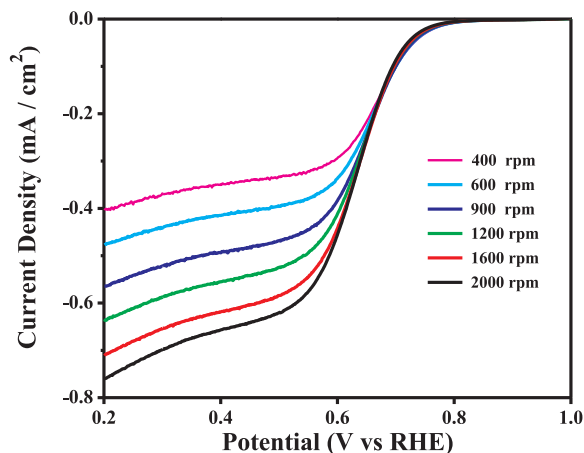
Fig. 6. RDE curves of R_{370}-CN at different rotation speeds in O_2-saturated 0.1M K$_2$SO$_4$.
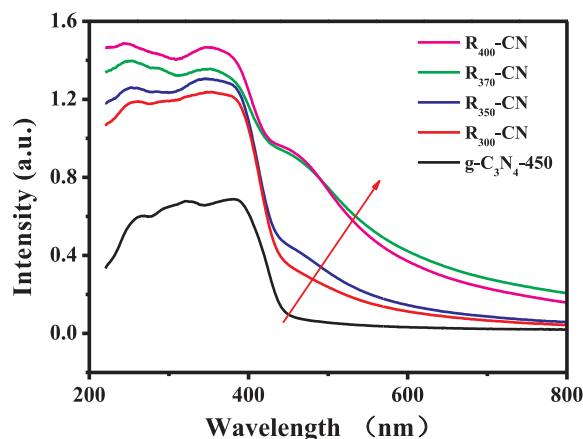
Fig. 7. UV–vis DRS of pristine g-C$_3$N$_4$-450 and R$_x$-CN (x = 300, 350, 370 and 400).

electronic bands structure and the separation of photoexcited carriers were carried out. The former could lead to a characteristic change in redox capability as well as in spectral absorption behavior of the photocatalyst, which was considered to be significant for photocatalytic generation of H_2O_2 from pure water.

3.5. Evaluation of band structure of the reduced g-C$_3$N$_4$-450

As shown in Fig. 7, the pristine g-C$_3$N$_4$-450 showed a weaker absorption capacity in the entire wavelength region examined in the UV–vis DRS, which was attributable to its poor characteristic nature towards polymerization [3]. The incorporation of the defects not only increased the intensity of absorbance of the catalyst in UV region, but also extended the absorption to more visible region. The spectral absorbance of the catalyst was enhanced with the reduction temperature. As suggested in an earlier work [22], the extent to which the light got absorbed with the reduced g-C$_3$N$_4$-450 could be attributed to the incorporation of C≡N into the catalyst. Tauch model as given below was used to calculate the optical band gap of the photocatalyst.

$$\alpha h\nu = D(h\nu - E_g)^n$$

Where $h\nu$ is the photon energy, E_g is the optical band gap, and D is a constant. For a direct transition, n is 1/2 [39,40].

The direct transition of the pristine g-C$_3$N$_4$-450 was estimated to be 443 nm and it moved from 446 to 492 nm as the reduction temperature went up from 300 to 400 °C (Fig. S7). The narrowed band gap upon the development of C≡N reflected in the color of the catalyst as well, and the color turned from white to brown on the basis of reduction temperature. Moreover, it is worth noting that a absorption shoulder observed at around 500 nm against g-C$_3$N$_4$-450, was an evident for an additional energy level that probably due to the introduction of nitride vacancies into the catalyst [23].

Mott-Schottky measurement was conducted to determine the position of VB and CB and identify the nature of reduced g-C$_3$N$_4$-450. As shown in Fig. S8, both the pristine and reduced g-C$_3$N$_4$-450 showed a typical n-type semiconductor behavior. Generally, the defect-modification has no impact on the nature of a semiconducting material [2,13,41]. The flat band potential was determined to be −1.208, −1.058, −0.860 and −0.520 V (vs Ag/AgCl) for g-C$_3$N$_4$-450, R$_{350}$-CN, R$_{370}$-CN and R$_{400}$-CN, respectively. The electronic band structure of the respective catalyst material could, therefore, be established from the potential of band gap energy. As schemed in Fig. S9, both the CB and VB levels of the reduced catalyst were more positive as compared to the pristine g-C$_3$N$_4$-450 and shifted to positive positions on increasing the reduction temperature. The extent of CB shifting was greater than that of VB shifting, which might render the catalyst with a capacity of water oxidation, as well as the O_2 reduction. A well optimized catalyst could
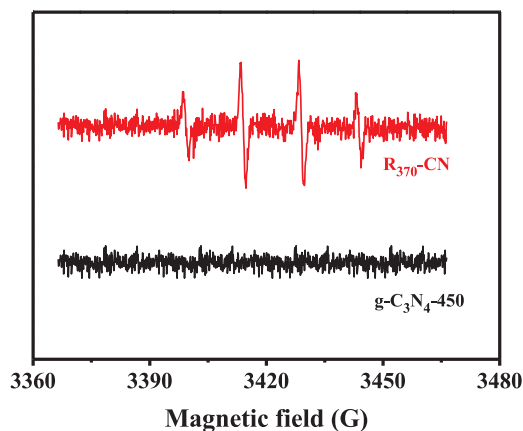
Fig. 8. DMPO spin-trapping EPR spectra for DMPO·-·OH of pristine g-C_3N_4-450 and R_{370}-CN.

be obtained, only when both the energy levels of VB and CB could promote water oxidation and O_2 reduction, respectively, which the R_{370}-CN material just was of the characteristics as the one previously reported [2,13].

3.6. Confirmation studies on modification of electronic band structure

To confirm further the shift of VB to the energy level of water oxidation upon the reduction treatment, ·OH that considered to be an important intermediate for the water oxidation, was detected in the reaction process through the trapping of ·OH by benzoic acid. As shown in Fig. S10, the amount of ·OH generated from the photocatalytic oxidation of pure water containing $AgNO_3$ as electron sacrifice, increased as the proceeding of photocatalysis, while for the pristine catalyst, it was insignificant. The results were further confirmed by the ·OH trapping-EPR analysis. As shown in Fig. 8, the EPR spectra with DMPO for the R_{370}-CN exhibited typical signals 1:2:2:1, in accordance with those of the DMPO-·OH [42]. In contrast, no such EPR signals were observed for the pristine catalyst. The photocatalytic generation of ·OH confirmed that the incorporation of defects such as C≡N altered the band gap and band energy level, rendering the VB with the energy of water oxidation.

The absorption shoulder of the reduced g-C_3N_4-450 (Fig. 7) might be originated from the development of an intermediate energy level upon the reduction treatment. To confirm the existence of the energy level and clarify its contribution to the efficiency of the photocatalytic H_2O_2 generation, a monochromatic light centered at 500 nm (Fig. S11a), much longer than the direct gap of R_{370}-CN (461 nm), was used as an irradiation light to conduct photocatalytic run. Compared with that of the pristine g-C_3N_4-450, the R_{370}-CN could still produce H_2O_2 by the monochromatic light longer than 485 nm, and the production efficiency was enhanced in the presence of isopropanol (Fig. S11b) as hole sacrifice. This result further confirmed the downshift of VB energy level, which moderately improved the oxidation performance towards both water and organic species such as isopropanol.

3.7. DFT calculations

The change in the band structure of the reduced g-C_3N_4-450 could be ascribed to the incorporation of electron acceptors such as C≡N functional groups into the structure of g-C_3N_4-450, which would delocalize the electron density of the highest occupied molecular orbital (HOMO) and lowest unoccupied molecular orbital (LUMO) on the same melem unit [32]. To clarify the effect theoretically, DFT was used to perform electronic structure calculations for the catalyst. The main electronic transitions of photoexcitation are expected to be from HOMO to LUMO. As described in Fig. S12, the introduction of C≡N functional

groups reduced the energy level of both HOMO and LUMO simultaneously, which was in good agreement with the experimental results. In the case of the melem model, the electron density on both HOMO and LUMO were located mainly on the melem moiety, which unfavored the separation of the photo-excited holes (h^+) and electrons (e^-) [14,43], resulting in the lower photocatalytic efficiency. The incorporation of C≡N functional group showed a high electrophilicity. Although the electrons on HOMO were not much changed and mainly located on the melem moiety, they deviated from melem to the C≡N group on LUMO. As a result, the preferred active sites of the reduced catalyst for oxidation reactions were located at the melem, while for reduction reactions, those were approaching to the C≡N group. Therefore, the introduction of C≡N group acted as electron acceptor that not only modified the electronic band structure but also separated the reduction and oxidation sites, resulting in the enhancement of photocatalytic activity.

3.8. PL emission spectrum analysis

The effective separation of photoexcited electrons and holes upon the reduction treatment was confirmed by PL emission spectrum analysis. As shown in Fig. 9, in contrast to a strong fluorescence emission peak at 490 nm observed for the pristine g-C_3N_4-450, a much quenched PL signals were observed against the reduced catalyst materials. Furthermore, the appearance of red shift with an increase of reduction temperature confirmed that the energy band gap got narrower [23,44]. Also, it is worth noting that quenching efficiency increased with the raise in reduction temperature, which indicated the far effective separation of electron and hole charges of the reduced catalyst prepared at higher temperature. Considering the quenching trend of PL, the R_{400}-CN could be an excellent candidate for the enhanced photogeneration of H_2O_2. However, a notable decline in the photogeneration was observed due to, otherwise the shortcoming in the electronic band energy structure mentioned above, i.e., the breaking-up of s-triazine that was already confirmed by both XPS and FTIR analysis. The reduction of melem units suppressed the formation of 1,4-endoperoxide species located at the 1,4-site of the melem unit [2], and consequently caused a decline in the photogeneration efficiency of H_2O_2.

3.9. Electrochemical impedance testing

EIS was performed with an aim of understanding the charge separation and their transfer at the solid-solution interface. As shown in Fig. 10, the R_{370}-CN showed a representative Nyquist plot with a much smaller arc radius than that of the pristine g-C_3N_4-450. Under visible light irradiation, the observed smaller arc radius indicated that the
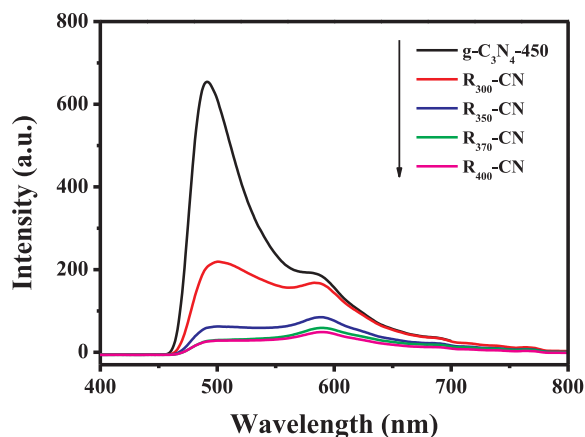

Fig. 9. Photoluminescence spectra excited at 310 nm for pristine g-C_3N_4-450 and R_x-CN (x = 300, 350, 370 and 400). (For interpretation of the references to colour in this figure legend, the reader is referred to the web version of this article.)
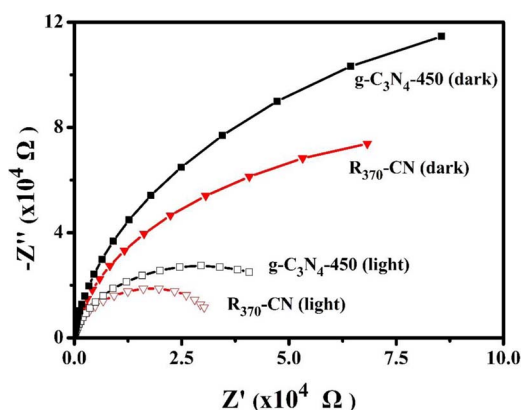
Fig. 10. Electrochemical impedance spectroscopy for pristine g-C$_3$N$_4$-450 and R$_{370}$-CN.

charge transfer resistance of g-C$_3$N$_4$-450 was remarkably decreased due to the development of the defects. The charge transfer was further promoted due to the photoexcitation that resulted in the enhanced photocatalytic activity of the reduced catalyst.

3.10. Stability of the R$_{370}$-CN photocatalyst

As shown in Fig. S13a, the catalytic performance remained fairly stable and the catalyst recovery could reach above 90% even after 4th run. The FTIR spectra of the fresh and used R$_{370}$-CN exhibited almost the identical peaks (Fig. S13b), particularly for the case of retainment of C≡N groups upon the reaction. A prolonged experimental run was performed for a maximum period of 10 h. The trend of H$_2$O$_2$ generation was linearly increased up to 8 h and gradually became an exponential in the last 2 h. The generated concentration of H$_2$O$_2$ was to a maximum of nearly 1mM at 10 h of the process (Fig. S14). The above results indicated that the R$_{370}$-CN was photocatalytically stable material.

4. Conclusion

The reduced g-C$_3$N$_4$-450 material was successfully prepared by a thermal treatment in presence of NaBH$_4$, that showed a highly enhanced visible light-driven photocatalytic performance on H$_2$O$_2$ generation from pure H$_2$O and O$_2$ at ambient atmosphere in the absence of organic electron donors. The reduction treatment could eliminate nitrides and open up the s-triazine heterocycles in g-C$_3$N$_4$-450 to develop defects such as nitride vacancies and C≡N functional groups. Both the instrumental characterization and theoretical calculations demonstrated that the defects developed could modify the electronic band structure of the catalyst. The incorporation of C≡N functional group not only shifted the CB and VB energy level down and narrowed the energy band gap of the reduced catalyst, but also deviated the electrons of LUMO from melem to the C≡N group, thereby separated the reduction and oxidation sites of the catalyst. The formation of nitride vacancies could introduce an intermediate energy level, that in turn extended the spectral absorption range of the prepared catalyst. The selective formation of H$_2$O$_2$ via the two-electron reduction reaction of O$_2$ was found to be predominant using the reduced g-C$_3$N$_4$–450 material, which was evaluated by RDE studies. The shifted VB energy level into the region of water oxidation capacity and the extended spectral absorption along with effective separation of the photoexcited carriers caused an highly enhanced photocatalytic performance on H$_2$O$_2$ generation from pure H$_2$O and O$_2$.

Acknowledgments

Appendix A. Supplementary data

Supplementary material related to this article can be found, in the online version, at doi:https://doi.org/10.1016/j.apcatb.2018.03.035.

References

[1] K. Mase, M. Yoneda, Y. Yamada, S. Fukuzumi, Nat Commun. 7 (2016) 11470.
[2] Y. Shiraishi, S. Kanazawa, Y. Kofuji, H. Sakamoto, S. Ichikawa, S. Tanaka, T. Hirai, Angew. Chem. Int. Ed. 53 (2014) 13454–13459.
[3] X. Wang, K. Maeda, A. Thomas, K. Takanabe, G. Xin, J.M. Carlsson, K. Domen, M. Antonietti, Nat. Mater. 8 (2009) 76–80.
[4] D. Masih, Y. Ma, S. Rohani, Appl. Catal. B Environ. 206 (2017) 556–588.
[5] Y. Shiraishi, S. Kanazawa, Y. Sugano, D. Tsukamoto, H. Sakamoto, S. Ichikawa, T. Hirai, ACS Catal. 4 (2014) 774–780.
[6] S. Yang, Y. Gong, J. Zhang, L. Zhan, L. Ma, Z. Fang, R. Vajtai, X. Wang, P.M. Ajayan, Adv Mater. 25 (2013) 2452–2456.
[7] Y. He, L. Zhang, B. Teng, M. Fan, Environ. Sci. Technol. 49 (2015) 649–656.
[8] S. Cao, J. Low, J. Yu, M. Jaroniec, Adv Mater. 27 (2015) 2150–2176.
[9] G. Tan, L. She, J. Yu, C. Xu, H. Ren, A. Xia, Appl. Catal. B Environ. 207 (2017) 120–133.
[10] L. Ge, C. Han, Appl. Catal. B Environ. 108–109 (2011) 100–107.
[11] X. Chen, J. Zhang, X. Fu, M. Antonietti, X. Wang, J. Am. Chem. Soc. 131 (2009) 11658–11659.
[12] Y. Shiraishi, Y. Kofuji, H. Sakamoto, S. Tanaka, S. Ichikawa, T. Hirai, ACS Catal. 5 (2015) 3058–3066.
[13] Y. Kofuji, S. Ohkita, Y. Shiraishi, H. Sakamoto, S. Tanaka, S. Ichikawa, T. Hirai, ACS Catal. 6 (2016) 7021–7029.
[14] S. Chu, Y. Wang, Y. Guo, J. Feng, C. Wang, W. Luo, X. Fan, Z. Zou, ACS Catal. 3 (2013) 912–919.
[15] J. Liu, Y. Liu, N. Liu, Y. Han, X. Zhang, H. Huang, Y. Lifshitz, S.T. Lee, J. Zhong, Z. Kang, Science 347 (2015) 970–974.
[16] Y. Wang, X. Wang, M. Antonietti, Angew. Chem. Int. Ed. Engl. 51 (2012) 68–89.
[17] W. Che, W. Cheng, T. Yao, F. Tang, W. Liu, H. Su, Y. Huang, Q. Liu, J. Liu, F. Hu, Z. Pan, Z. Sun, S. Wei, J. Am. Chem. Soc. 139 (2017) 3021–3026.
[18] Y. Kofuji, Y. Isobe, Y. Shiraishi, H. Sakamoto, S. Tanaka, S. Ichikawa, T. Hirai, J. Am. Chem. Soc. 138 (2016) 10019–10025.
[19] S. Li, G. Dong, R. Hailili, L. Yang, Y. Li, F. Wang, Y. Zeng, C. Wang, Appl. Catal. B Environ. 190 (2016) 26–35.
[20] M.Y. Ye, Z.H. Zhao, Z.F. Hu, L.Q. Liu, H.M. Ji, Z.R. Shen, T.Y. Ma, Angew. Chem. Int. Ed. Engl. 56 (2017) 8407–8411.
[21] Y. Li, S. Ouyang, H. Xu, X. Wang, Y. Bi, Y. Zhang, J. Ye, J. Am. Chem. Soc. 138 (2016) 13289–13297.
[22] G. Liu, G. Zhao, W. Zhou, Y. Liu, H. Pang, H. Zhang, D. Hao, X. Meng, P. Li, T. Kako, J. Ye, Adv. Funct. Mater. 26 (2016) 6822–6829.
[23] P. Niu, L.C. Yin, Y.Q. Yang, G. Liu, H.M. Cheng, Adv Mater. 26 (2014) 8046–8052.
[24] D. Cheng, S. Yuan, P. Liao, P. Zhang, Environ Sci Technol. 50 (2016) 11646–11653.
[25] H. Zhou, X. Zou, K. Zhang, P. Sun, M.S. Islam, J. Gong, Y. Zhang, J. Yang, ACS Appl Mater Interfaces. 9 (2017) 18699–18709.
[26] G. Liu, P. Niu, C. Sun, S. Smith, Z. Chen, G. Lu, H. Cheng, J. Am. Chem. Soc. 13 (2010) 11642–11648.
[27] P. Niu, L. Zhang, G. Liu, H.-M. Cheng, Adv. Funct. Mater. 22 (2012) 4763–4770.
[28] S. Chu, C. Wang, J. Feng, Y. Wang, Z. Zou, Int. J. Hydrogen Energy 39 (2014) 13519–13526.
[29] G.-h. Moon, M. Fujitsuka, S. Kim, T. Majima, X. Wang, W. Choi, ACS Catal. 7 (2017) 2886–2895.
[30] M. Groenewolt, M. Antonietti, Adv. Mater. 17 (2005) 1789–1792.
[31] B.V. Lotsch, M. Doblinger, J. Sehnert, L. Seyfarth, J. Senker, O. Oeckler, W. Schnick, Chemistry 13 (2007) 4969–4980.
[32] Y. Kang, Y. Yang, L.C. Yin, X. Kang, G. Liu, H.M. Cheng, Adv Mater. 27 (2015) 4572–4577.
[33] G. Zhang, S. Zang, X. Wang, ACS Catal. 5 (2015) 941–947.
[34] S. Bayan, A. Midya, N. Gogurla, A. Singha, S.K. Ray, The J. Physical Chemistry C. 121 (2017) 19383–19391.
[35] R. Wang, S. Ni, G. Liu, X. Xu, Appl. Catal. B Environ. 225 (2018) 139–147.
[36] Y. Kofuji, S. Ohkita, Y. Shiraishi, H. Sakamoto, S. Ichikawa, S. Tanaka, T. Hirai, ACS Sustainable Chemistry & Engineering. 5 (2017) 6478–6485.
[37] S. Zhao, X. Zhao, H. Zhang, J. Li, Y. Zhu, Nano Energy. 35 (2017) 405–414.
[38] P. Singh, D.A. Buttry, The J. Physical Chemistry C. 116 (2012) 10656–10663.
[39] J. Li, B. Shen, Z. Hong, B. Lin, B. Gao, Y. Chen, Chem Commun. 48 (2012) 12017–12019.
[40] S.T. Tan, B.J. Chen, X.W. Sun, W.J. Fan, H.S. Kwok, X.H. Zhang, S.J. Chua, J. Appl. Phys. 98 (2005) 013505.
[41] T.F. Yeh, C.Y. Teng, S.J. Chen, H. Teng, Adv Mater. 26 (2014) 3297–3303.
[42] J. Zhao, T. Wu, K. Wu, K. Oikawa, H. Hidaka, A. Serpone, Environ. Sci. Technol. 32 (1998) 2394–2400.
[43] X. Fan, L. Zhang, R. Cheng, M. Wang, M. Li, Y. Zhou, J. Shi, ACS Catal. 5 (2015) 5008–5015.
[44] Y. Kang, Y. Yang, L.C. Yin, X. Kang, L. Wang, G. Liu, H.M. Cheng, Adv Mater. 28 (2016) 6471–6477.